

Optimization of Solar Tower molten salt cavity receivers for maximum yield based on annual performance assessment

Peter Schöttl*, Gregor Bern, De Wet van Rooyen, José Antonio Fernández Pretel, Thomas Fluri, Peter Nitz

Fraunhofer Institute for Solar Energy Systems ISE, Heidenhofstrasse 2, D-79110 Freiburg, Germany

ARTICLE INFO

Keywords:

Central receiver solar tower systems
Cavity receiver optimization
Transient simulation
Annual yield assessment
Evolutionary algorithm

ABSTRACT

The receiver at the optical-to-thermo-hydraulic interface of a Solar Tower plant needs careful optimization in the design stage to guarantee maximum yield during operation. Due to the highly transient behavior of a Solar Tower plant, evaluation of the receiver performance based on annual yield as a figure of merit is important. In this study, a novel method for the optimization of Solar Tower molten salt cavity receivers is introduced, which integrates optical, thermal, hydraulic and operational aspects. The receiver geometry, the hydraulic layout and the aiming strategy are optimized simultaneously. The optimization objective function is based on a validated simulation model that integrates a *sky discretization approach* for optical assessment and an *Artificial Neural Network* for fast system simulation. This approach allows to accelerate the transient annual assessment such that annual thermal yield can be used as figure of merit in the iterative optimization. For the latter, an *Evolutionary Algorithm* adapted to the problem has been applied, which allows for identifying optimized receiver configurations with reasonable computational effort.

The methodology is demonstrated by means of a 55 MW_{th} receiver and a given Heliostat Field in southern Spain. For this example, the evolution of receiver parameters during the course of the optimization and the break-down of different loss contributions are discussed. The optimized receiver configuration delivers more than 4% higher annual yield, as compared to the reference configuration based on static design considerations. The approach's applicability to different systems – external receivers, other heat transfer fluids, commercial scale system sizes – is discussed.

1. Introduction

The solar receiver of a Central Receiver Solar Tower plant (CRS) is the optical and thermo-hydraulic interface, which couples the *Heliostat Field* (HSF) to the storage and power generation systems. According to Kolb et al. (2011), the solar receiver (in the following referred to as *receiver*) and the tower account for about 20 % of the plant investment costs. Furthermore, the solar-to-thermal efficiency of the receiver directly influences the required size of the HSF, with the latter being responsible for about 40 % of the plant investment costs (Kolb et al., 2011). Therefore, a careful optimization of the receiver geometry – taking into account its interactions with the other plant components – is crucial.

As a receiver has significantly different characteristics compared to conventional heat exchangers, several aspects of its design need particular attention. Amongst others are:

- high material stresses due to high solar flux concentration and its potential inhomogeneities
- highly transient behavior of the solar radiation
- trade-off between optical and thermal losses
- trade-off between pressure losses and good heat transfer characteristics

In this study, a receiver optimization methodology is presented, which takes into account major design aspects like receiver geometry, hydraulic flow of the *Heat Transfer Fluid* (HTF) and aiming strategy. While the methodology is demonstrated for the special case of molten salt cavity receivers, its applicability to other cases is discussed as well.

The basic receiver geometry is depicted in Fig. 1. Several panels with parallel-aligned tubes form a quasi-cylindrical cavity, which is covered at the bottom and the top. The front aperture is partly closed by an upper lip, which creates a zone of stagnant air in the upper part of the cavity (see Section 2.1.3) and thereby reduces the convective losses.

* Corresponding author.

E-mail address: peter.schoettl@ise.fraunhofer.de (P. Schöttl).

<https://doi.org/10.1016/j.solener.2020.02.007>

Received 5 January 2019; Received in revised form 20 January 2020; Accepted 2 February 2020

0038-092X/ © 2020 The Authors. Published by Elsevier Ltd on behalf of International Solar Energy Society. This is an open access article under the CC BY license (<http://creativecommons.org/licenses/by/4.0/>).

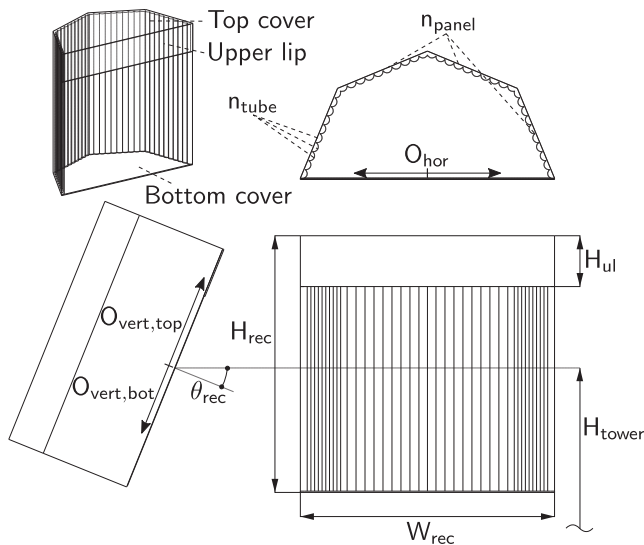


Fig. 1. Basic receiver geometry: several tube-panels (n_{panel} panels with n_{tube} tubes each) form a cavity in the shape of a half-cylinder, which is closed with covers at the bottom and the top. The cylinder's aperture has the width W_{rec} and the height H_{rec} . A small part at the top of the aperture is covered with the upper lip of height H_{ul} . The aperture normal may not be horizontal, but instead point downwards with a given receiver inclination angle θ_{rec} . The receiver is located on top of a tower, with the aperture center being at height H_{tower} . Three maximum offsets of the outermost aim points from the aperture center characterize the aiming strategy: horizontal aim point offset O_{hor} , top vertical aim point offset $O_{\text{vert,top}}$ and bottom vertical aim point offset $O_{\text{vert,bottom}}$.

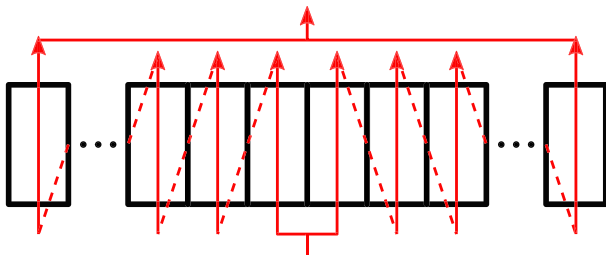


Fig. 2. HTF flow (red arrows) pattern through the receiver panels (black). The HTF stream is split in two flow paths, which enter at the innermost panels. Subsequently, the flow paths go through the western and eastern panels respectively and leave at the outermost ones. The flow is not meandering, i.e. the HTF always enters at the bottom of a panel, leaves at the top and flows to the bottom of the next panel behind the absorber surfaces (dashed lines). (For interpretation of the references to colour in this figure legend, the reader is referred to the web version of this article.)

speed and capability to find the maximum for the objective function. An optimization of the entire Solar Tower plant is performed by Augsburger (2013), where the width and height of external receivers are taken into account as *degrees of freedom* (DoF). Craig et al. (2014) suggest an optimization approach for hybrid pressurized air receivers based on *computational fluid dynamics*. Carrizosa et al. (2015) investigate systems with multiple cavity receivers and propose an alternating iterative optimization of HSF and receiver. Augsburger et al. (2016) present an optimization methodology for external molten salt receivers, where different potential solutions are ranked according to multiple weighted design criteria. Wang et al. (2017) discuss the optimization of a variable distribution of the receiver surface solar absorptance to obtain a Pareto front between homogenization of absorbed solar flux and reflection losses. Beyond the CRS domain, both Asselineau et al. (2015) and Zou et al. (2017) describe a geometry optimization of cavity receivers for parabolic dish systems.

In contrast to existing literature, this study uses detailed transient optical and thermo-hydraulic modeling, but also presents a method that permits fast annual assessment of the receiver in the power plant context. This implies that the receiver's dynamic interactions with the HSF and the thermal-to-electric power conversion system are taken into account during the optimization. In this way, the presented optimization approach is more realistic than strategies which are based on mere design point considerations.

1.2. Structure of this study

Following the introduction, the optimization methodology is described in Section 2. This comprises a detailed description of all simulation components of the objective function and an explanation of the algorithmical optimization approach. In Section 3, the application of the developed methodology is demonstrated by means of an example case. The results of the optimization of the respective receiver are presented and the applicability to other scenarios is discussed. Section 4 summarizes the study and outlines potential future enhancements. In the appendix, the simulation model is validated (Appendix A) and a sensitivity analysis for the exemplarily optimized receiver configuration is presented (Appendix B).

2. Optimization methodology

As depicted in Fig. 3, the objective function for the optimization is structured in two main parts: the *Detailed Physical Model* (DPM) and the annual simulation model based on an *Artificial Neural Network* (ANN). All components of both parts are described in the following. Furthermore, the optimization approach based on an *Evolutionary Algorithm* (EA) is explained in Section 2.4.

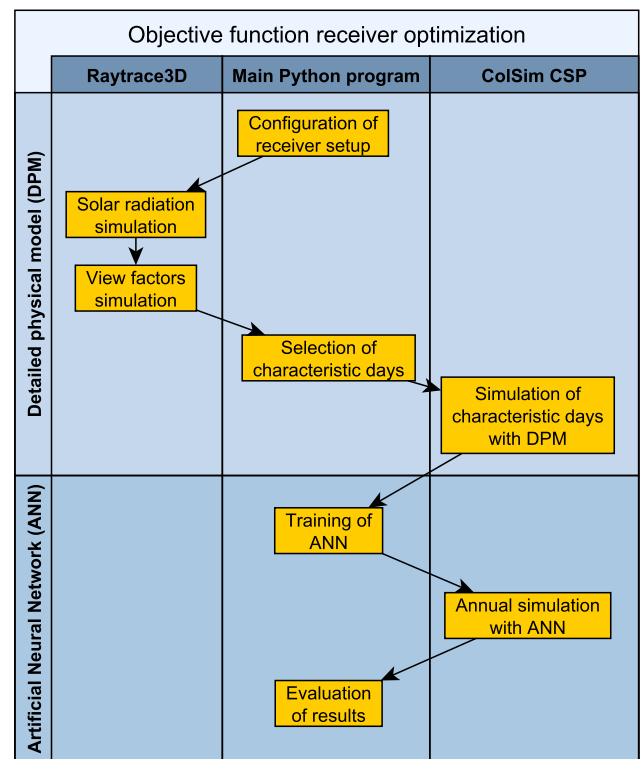


Fig. 3. Flow chart of the objective function for the optimization, including a *Detailed Physical Model* and an annual simulation model based on an *Artificial Neural Network*. The Fraunhofer ISE-tools *Raytrace3D* and *ColSim CSP* are integrated for various tasks along the tool chain.

2.1. Detailed Physical Model

Parts of the DPM have been published before. To facilitate comprehension of the overall optimization toolchain, these parts are summarized subsequently. Other – previously unpublished – aspects of the DPM are covered in detail.

The DPM is implemented as a component model in the *Fraunhofer ISE* in-house system simulation tool *ColSim CSP* (Wittwer, 1999). The time step size throughout the simulation is 60 s. A convergence investigation within this study has demonstrated that differences from using smaller time steps are negligible.

For validation purposes, a comparison of simulation results and measurement data from the Solar Two project (Pacheco et al., 2002) has been performed, which is described in Appendix A.

2.1.1. Solar radiation and aiming strategy

The distribution of solar radiation flux on the absorber surfaces of the receiver is modeled with the *Fraunhofer ISE* in-house ray tracing engine *Raytrace3D* (Branke and Heimsath, 2010; Heimsath et al., 2014). The geometric representation in the ray tracing scene includes the cylindrical curvature of the absorber tubes. The cell size of the flux map discretization is equal to the arc length of one tube’s half cylinder (see Fig. 5). As the tube surfaces have an absorptance smaller than 100%, a part of the incident solar radiation is assumed to be diffusely reflected either onto other surfaces in the cavity or towards the environment. These secondary reflections are handled as part of the ray tracing routine.

To homogenize the flux distribution on the cavity surfaces, an aiming strategy is applied that assigns an aim point to each heliostat, depending on the sun position and the required integral flux on the receiver (Schöttl et al., 2018). These aim points are distributed on an equidistant grid on the aperture plane of the cavity, with 7 and 5 levels in horizontal and vertical directions respectively. The maximum offsets of the outermost aim points (left, right, top, bottom) can be individually defined (see Fig. 1). Heliostats far away are assigned to aim points in the lower regions of the aperture, while heliostats close to the tower aim at the upper section. The west part of the solar field is assigned to aim points on the east side of the aperture and vice versa. Such assignments ensure that the part of the cavity at which a heliostat aims is oriented towards the heliostat and therefore reduce spillage. As the HSF is symmetric with respect to the north–south axis, one maximum horizontal aim point offset O_{hor} is used in both directions. Due to the upper lip, the receiver inclination and the different focal spot sizes of close and far heliostats, a separate value for the maximum top vertical aim point offset $O_{vert,top}$ and the maximum bottom vertical aim point offset $O_{vert,bottom}$ is used. The optima for the maximum aim point offsets are highly dependent on the receiver geometry and are therefore subject to optimization.

The solar radiation is highly transient, with variations due to current *Direct Normal Irradiance* (DNI), sun position and aiming strategy. To account for these transients, a *sky discretization* approach (Schöttl et al., 2016) and a flux map interpolation with *Radial Basis Function* correction (Schöttl et al., 2018) is applied. This approach does not include cloud passages and partial covering of the HSF, which is assumed to not have an impact on the optimum receiver configuration as derived in this study.

The model allows to calculate an individual absorbed solar flux $\dot{Q}_{sol,abs,i}^{(t)}$ for each exposed surface element i in the cavity at each time step (t) . Furthermore, the solar optical losses for the entire receiver can be calculated as

$$\dot{Q}_{loss,sol}^{(t)} = G_{bn}^{(t)} \cdot A_{HSF} - \dot{Q}_{sol,abs}^{(t)} \quad (1)$$

with DNI G_{bn} , HSF net mirror area A_{HSF} and integral absorbed solar flux $\dot{Q}_{sol,abs}^{(t)} = \sum_i \dot{Q}_{sol,abs,i}^{(t)}$.

2.1.2. Thermal radiation heat transfer

To model thermal radiation heat transfer between surfaces in the cavity and towards the environment, a *view factor*-based approach as presented by Teichel et al. (2012) has been implemented. The view factors for the surfaces in the cavity are derived with ray tracing.

All surfaces in the cavity are assumed to be fully diffuse and to have a temperature-independent IR emittance ϵ_{surf} . The tubes on the panels are modeled with cylinders, while the passive surfaces in the cavity (top/bottom cover, upper lip) are flat. To estimate the emitted radiation of a surface, its temperature from the last simulation time step is taken into account. This simplification is justified due to the small time step size and the surface temperature in the cavity being dominated by the solar radiation. The model allows to calculate an individual thermal radiation absorbed heat flux $\dot{Q}_{tr,abs,i}^{(t)}$ and thermal radiation emitted heat flux $\dot{Q}_{tr,em,i}^{(t)}$ for each exposed surface element i in the cavity at each time step (t) . These sum up to the thermal radiation loss $\dot{Q}_{tr,i}^{(t)} = \dot{Q}_{tr,em,i}^{(t)} - \dot{Q}_{tr,abs,i}^{(t)}$. Details about the mathematical implementation of the method are given by Schöttl et al. (2017).

Computationally intensive, but temperature-independent parts of the radiation exchange calculation are performed only once at the beginning of the simulation. This is advantageous in a dynamic simulation, as less calculations have to be performed each time step.

2.1.3. Convective heat transfer

The convective heat transfer between cavity surfaces, bulk air in the cavity and surrounding air is calculated with a two-zone model as introduced by Clausing (1983): convective losses occur in the *convective zone* in the lower part of the cavity, while convective heat transfer in the *stagnant zone* in the upper part of the cavity is suppressed. The dimensions of the upper lip have significant influence on the size of the stagnant zone. Both zones are depicted in Fig. 4.

The model considers wind influence and takes the cavity inclination into account. It allows to calculate an individual convective heat transfer coefficient $\alpha_i^{(t)}$ and consequently a convective heat flux $\dot{Q}_{conv,i}^{(t)}$ for each exposed surface element i in the cavity at each time step (t) . Details about the implementation are given by Schöttl et al. (2017).

As compared to the receiver type studied herein, the Clausing model was created for deeper cavities (smaller aperture as compared to the overall absorber area). Furthermore, it is based on many assumptions and an uncertainty assessment is not available (Clausing, 1983). Thus, large uncertainties with regard to convective loss assessment within this study are expected. While the authors are not aware of more accurate convection models with similar computational cost, other correlations might be integrated analogously.

2.1.4. Tube model

The tube model represents the interface between the energy fluxes at the active receiver surfaces (absorbed solar radiation, thermal

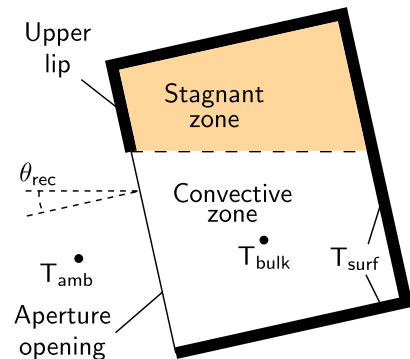


Fig. 4. Stagnant and convective zones (adapted from Clausing (1983)). Surface temperatures $T_{surf,i}$ and bulk temperature T_{bulk} are calculated with ambient temperature T_{amb} as input.

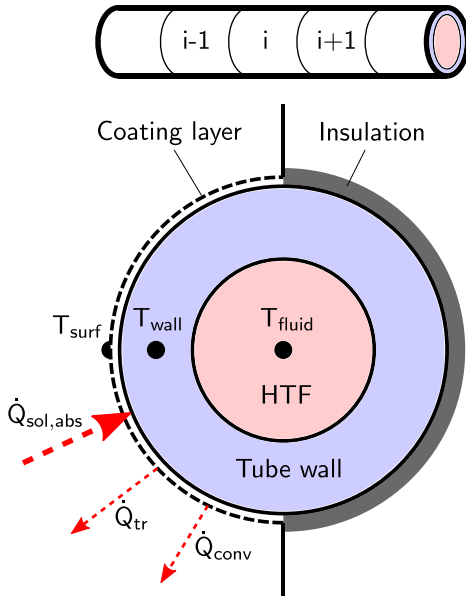


Fig. 5. Tube model with n axial nodes and a fluid and wall node in radial direction. The balance of absorbed solar radiation, thermal radiation losses and convective losses defines the heat flux into the wall node. The coating layer on the front side is only considered in terms of thermal conductivity, its heat capacity is neglected. The back side of the tube is adiabatic.

radiation, convective exchange) and the heat flux to the HTF. Tubes are built from stainless steel and have a black paint coating with high solar absorptance on their irradiated front side.

The tube model is based on several assumptions:

- According to literature (Kim et al., 2015; Teichel et al., 2012; Yang et al., 2012), receivers can be designed with an appropriate thermal insulation, such that thermal losses through the receiver backside are neglected.
- Compared to thermal conduction in radial direction, circumferential and axial heat conduction is negligibly small (Flesch et al., 2017).
- While the heat capacity of the coating can be neglected, its heat conductivity has to be taken into account.
- During normal operation, the tube surface temperature is dominated by the absorbed solar radiation.
- Time step size is small and thermal material properties can be approximated based on the temperature of the last time step.

Based on these assumptions, a tube model discretized in axial and radial direction (see Fig. 5) is created. The axial discretization uses n segments, with each segment being radially partitioned in a fluid node and a wall node. The latter is placed at the logarithmic mean radius (Kiefer, 2013). While the wall node represents the thermal capacity of the full cylindrical wall segment, only half of the inner and outer surfaces (front side) is used for heat exchange. The back side is adiabatic. The discretization and modeling is similar to the approach presented by Flesch et al. (2017), with the main difference being the adiabatic insulation of the tube backside.

In the following, the heat transfer for one tube segment i (equally being one surface element in the cavity) at time step (t) is described.

The surface heat flux is a balance of absorbed solar radiation, thermal radiation losses and convective losses:

$$\dot{Q}_{out,i}^{(t)} = \dot{Q}_{sol,abs,i}^{(t)} - \dot{Q}_{tr,i}^{(t)} - \dot{Q}_{conv,i}^{(t)} \quad (2)$$

The thermal resistance $R_{out,i}^{(t)}$ from the surface to the wall node is calculated according to heat conduction in cylindrical shells as

$$R_{out,i}^{(t)} = \frac{\frac{\ln(r_{out}/(r_{out} - \delta_{coat}))}{\lambda_{coat}} + \frac{\ln((r_{out} - \delta_{coat})/r_{wall})}{\lambda_{wall,i}^{(t)}}}{\pi \cdot \Delta L} \quad (3)$$

with outer radius r_{out} of wall and coating, coating thickness δ_{coat} , coating heat conductivity λ_{coat} , wall node radius r_{wall} , temperature-dependent wall heat conductivity $\lambda_{wall,i}^{(t)}$ and axial tube segment length ΔL .

The thermal resistance $R_{in,i}^{(t)}$ from the wall node to the fluid node is calculated as

$$R_{in,i}^{(t)} = \frac{\frac{1}{\alpha_{in,i}^{(t)}} + \frac{r_{in} \cdot \ln(r_{wall}/r_{in})}{\lambda_{wall,i}^{(t)}}}{\pi \cdot \Delta L \cdot r_{in}} \quad (4)$$

with inner tube radius r_{in} and convective heat transfer coefficient $\alpha_{in,i}^{(t)}$ from the inner tube wall to the HTF calculated with the Gnielinski correlation (VDI-GVC, 2010). Typically, $R_{in,i}^{(t)}$ is dominated by the convective heat transfer, which makes it also much larger than $R_{out,i}^{(t)}$.

For the calculation of the wall temperature $T_{wall,i}$, an internal energy balance is derived for the wall node:

$$\frac{\Delta U_{wall,i}^{(t)}}{\Delta t} = \dot{Q}_{out,i}^{(t)} - \dot{Q}_{HTF,i,estim}^{(t)} \quad (5)$$

with the time step size Δt . Inserting wall mass $m_{wall,i}$, wall specific heat capacity $c_{p,i}^{(t-1)}$ and temperatures in Eq. 5 yields

$$\frac{m_{wall,i} \cdot c_{p,i}^{(t-1)} (T_{wall,i}^{(t)} - T_{wall,i}^{(t-1)})}{\Delta t} = \dot{Q}_{out,i}^{(t)} - \frac{T_{wall,i}^{(t)} - T_{HTF,i}^{(t-1)}}{R_{in,i}^{(t)}} \quad (6)$$

After solving for $T_{wall,i}^{(t)}$, the respective internal energy $U_{wall,i}^{(t)} = f(T_{wall,i}^{(t)})$ is calculated. To guarantee energy conservation, the actual heat flux to the HTF is calculated with

$$\dot{Q}_{HTF,i}^{(t)} = \dot{Q}_{out,i}^{(t)} - \frac{U_{wall,i}^{(t)} - U_{wall,i}^{(t-1)}}{\Delta t} \quad (7)$$

The new surface temperature $T_{surf,i}^{(t)}$ can be derived as

$$T_{surf,i}^{(t)} = \dot{Q}_{out,i}^{(t)} \cdot R_{out,i}^{(t)} + T_{wall,i}^{(t)} \quad (8)$$

The film temperature $T_{film,i}^{(t)}$ – being the highest HTF temperature in one node – is computed as

$$T_{film,i}^{(t)} = \dot{Q}_{HTF,i}^{(t)} \cdot R_{HTF,i}^{(t)} + T_{HTF,i}^{(t-1)} \quad (9)$$

with $R_{HTF,i}^{(t)} = (\alpha_{in,i}^{(t)} \cdot \pi \cdot L \cdot r_{in})^{-1}$.

Based on $\dot{Q}_{HTF,i}^{(t)}$ and using a plug-flow approach (Wittwer, 1999), the HTF flow inside the tube from segment to segment is modeled. By comparing the HTF state at the inlet and outlet of the receiver, the power $\dot{Q}_{gain}^{(t)}$ to the HTF can be assessed.

2.1.5. Passive surfaces

Apart from the absorber panels, there are several passive surfaces in the cavity, which absorb and reflect solar radiation and participate in the thermal radiation and convective heat transfer. These surfaces are the top and bottom cavity covers and the upper lip (see Fig. 1). It is assumed that these surfaces are well insulated (Kim et al., 2015; Teichel et al., 2012) and therefore adiabatic.

Based on these assumptions, a steady-state heat balance is solved every time step (t) to derive the temperature $T_{surf,i}^{(t)}$ of the passive surface element i .

$$0 = \dot{Q}_{sol,abs,i}^{(t)} + \dot{Q}_{tr,abs,i}^{(t-1)} - \dot{Q}_{tr,em,i}^{(t)} + \dot{Q}_{conv,i}^{(t-1)} \quad (10)$$

$$0 = \dot{Q}_{sol,abs,i}^{(t)} + \dot{Q}_{tr,abs,i}^{(t-1)} - \epsilon_{surf,i} \cdot A_{surf,i} \cdot \sigma \cdot T_{surf,i}^{(t)4} + \alpha_{surf,i}^{(t-1)} \cdot A_{surf,i} \cdot (T_{bulk}^{(t-1)} - T_{surf,i}^{(t)}) \quad (11)$$

with Stefan–Boltzmann constant σ , surface emissivity $\epsilon_{surf,i}$ in the IR spectrum, convective heat transfer coefficient $\alpha_{surf,i}^{(t-1)}$ based on last timestep's temperatures and area $A_{surf,i}$ of the passive surface element i .

This is a quartic function whose four roots can be found analytically. Only one root yields a non-negative, non-imaginary solution which is accepted for $T_{\text{surf},i}^{(t)}$.

2.1.6. Pressure losses

Two effects cause pressure losses of the HTF. Firstly, hydrostatic pressure losses Δp_{stat} occur, as the receiver is mounted at a given height over the ground, up to which the molten salt has to be pumped against gravity. The maximum geodetic suction height is much lower than H_{tower} . Thus, the HTF in the downcomer flowing back to ground level cannot suck the HTF in the riser and its potential energy is effectively lost. Modeling Δp_{stat} is straightforward:

$$\Delta p_{\text{stat}}^{(t)} = \rho_{\text{HTF}} \cdot g \cdot H_{\text{tower}} \quad (12)$$

with

- the density ρ_{HTF} of the HTF at inlet temperature
- the gravitational constant g

Secondly, hydrodynamic pressure losses Δp_{dyn} occur due to friction in the absorber tubes and other hydraulic components of the receiver. Rodríguez-Sánchez et al. (2014) suggest modeling the pressure losses in the straight and elbow sections of the absorber tubes and in the contraction/expansion from header to absorber tubes and vice versa. A preliminary estimation for the reference design (see Table 2, $d_{\text{in}} = 2.1\text{cm}$) at nominal mass flow rate, with the same elbow sections (two 30° and one 120° elbow) and with the same ratio of elbow curvature radius to inner tube diameter as used by Rodríguez-Sánchez et al. (2014) has been conducted. The resulting shares of the hydrodynamic pressure loss were 81.6%, 14.1% and 4.3 % for straight tubes, expansion/contraction and elbow sections respectively. Based on these findings, the contribution from elbow sections is considered to be negligible and is not taken into account in the following calculations.

The hydrodynamic pressure losses are then calculated as

$$\Delta p_{\text{dyn}}^{(t)} = \sum_{\text{abs.tubes}} f_r^{(t)} \cdot \frac{H_{\text{rec}}}{2 \cdot r_{\text{in}}} \cdot \frac{\rho_{\text{HTF}}^{(t)}}{2} \cdot v_{\text{HTF}}^{2(t)} + \sum_{\text{expansions}} K_{\text{exp}} \cdot \frac{\rho_{\text{HTF}}^{(t)}}{2} \cdot v_{\text{HTF}}^{2(t)} + \sum_{\text{contractions}} K_{\text{con}} \cdot \frac{\rho_{\text{HTF}}^{(t)}}{2} \cdot v_{\text{HTF}}^{2(t)} \quad (13)$$

with Darcy friction factor $f_r^{(t)}$, expansion/contraction coefficients K_{exp} and K_{con} and HTF velocity $v_{\text{HTF}}^{(t)}$ modeled according to VDI-GVC (2010). For the latter, the mean value of the velocities in the header and absorber tubes is used. The cross-section area of the panel header tubes, which is required for calculation of K_{exp} and K_{con} , is assumed to be equal to the cumulative cross-section area of the panel's absorber tubes: $A_{\text{header}} = n_{\text{tube}} \cdot \pi \cdot r_{\text{in}}^2$. The total pressure losses are then calculated as $\Delta p_{\text{tot}}^{(t)} = \Delta p_{\text{stat}}^{(t)} + \Delta p_{\text{dyn}}^{(t)}$.

To avoid having a multi-objective optimization problem, the pressure losses are represented with a thermal energy equivalent, which can be set off against the energy $\dot{Q}_{\text{gain}}^{(t)}$ to the HTF. By introducing a constant pump efficiency $\eta_{\text{pump}} = 0.7$ (Rodríguez-Sánchez et al., 2014) and a constant thermal-to-electric conversion efficiency $\eta_{\text{th-el}} = 0.4$, an equivalent thermal pumping power $\dot{Q}_{\text{pump,th}}$ can be calculated:

$$\dot{Q}_{\text{pump,th}}^{(t)} = \frac{P_{\text{pump,el}}^{(t)}}{\eta_{\text{th-el}}} = \frac{\dot{m}_{\text{HTF}}^{(t)} \cdot \Delta p_{\text{tot}}^{(t)}}{\eta_{\text{th-el}} \cdot \eta_{\text{pump}} \cdot \rho_{\text{HTF}}^{(t)}} \quad (14)$$

Using a constant pump efficiency and thermal-to-electric conversion efficiency is a significant simplification compared to the level of detail of the majority of the DPM. This is justified, as the focus is on receiver optimization and simplification inaccuracies are equally applied to all compared configurations of the receiver.

2.1.7. Minimum mass flow rate and control approach

To avoid hot spots and material overstress, the heat transfer from

the absorber tube surfaces to the HTF must be sufficient during all operating conditions. Therefore, it is assumed that the tube flow must be fully turbulent, which holds for Reynolds numbers $\text{Re}_{\text{crit}} > 10^4$ (VDI-GVC, 2010). This criterion is in accordance with the findings of Benoit et al. (2016). From this condition, a minimum fluid velocity $v_{\text{HTF,min}}$ and a minimum mass flow rate \dot{m}_{min} can be calculated:

$$\dot{m}_{\text{min}} = A_{\text{HTF}} \cdot \rho_{\text{HTF}} \cdot v_{\text{HTF,min}} = A_{\text{HTF}} \cdot \frac{\text{Re}_{\text{crit}} \cdot \mu_{\text{HTF}}}{2 \cdot r_{\text{in}}} \quad (15)$$

with

- HTF flow cross-section area $A_{\text{HTF}} = \pi \cdot r_{\text{in}}^2 \cdot n_{\text{tube}} \cdot 2$ (two flow paths)
- dynamic viscosity μ_{HTF} of the HTF at the inlet

To determine the potential mass flow rate \dot{m}_{pot} through the receiver, an energy balance from inlet to outlet is derived:

$$\dot{Q}_{\text{gain,pot}}^{(t)} = \dot{m}_{\text{pot}}^{(t)} \cdot (h_{\text{outlet}} - h_{\text{inlet}}) \quad (16)$$

with inlet and outlet enthalpies $h_{\text{inlet}} = f(T_{\text{HTF,inlet}})$ and $h_{\text{outlet}} = f(T_{\text{HTF,outlet}})$ respectively. The potential power $\dot{Q}_{\text{gain,pot}}^{(t)}$ to the HTF is estimated with the potential absorbed solar radiation $\dot{Q}_{\text{sol,abs,pot}}^{(t)}$ and the thermal losses from the last time step $\dot{Q}_{\text{loss,th}}^{(t-1)}$:

$$\dot{Q}_{\text{gain,pot}}^{(t)} = \dot{Q}_{\text{sol,abs,pot}}^{(t)} - \dot{Q}_{\text{loss,th}}^{(t-1)} \quad (17)$$

The flux map interpolation and the heliostat defocusing approach – as introduced in Section 2.1.1 and by Schöttl et al. (2018) – allow for limiting the flux such that the potential absorbed radiation is cut off at the design load ($\dot{Q}_{\text{sol,abs,pot}}^{(t)} \leq \dot{Q}_{\text{sol,abs,design}}^{(t)}$). This also defines dumping losses $\dot{Q}_{\text{loss,dump}}^{(t)}$, which are equivalent to the cut-off power due to the design load restriction.

To guarantee safe operation and avoid oscillations, the controller takes into account a hysteresis of 50% for the determination of the mass flow rate $\dot{m}^{(t)}$ for the current time step, if the mass flow rate $\dot{m}^{(t-1)}$ of the last time step is zero.

$$\dot{m}^{(t)} = \begin{cases} \dot{m}_{\text{pot}}^{(t)} & \text{if } \dot{m}^{(t-1)} > 0 \wedge \dot{m}_{\text{pot}} > \dot{m}_{\text{min}} \\ \dot{m}_{\text{pot}}^{(t)} & \text{if } \dot{m}^{(t-1)} = 0 \wedge \dot{m}_{\text{pot}} > \dot{m}_{\text{min}} \cdot 1.5 \\ 0 & \text{otherwise} \end{cases} \quad (18)$$

This means that \dot{m}_{pot} has to surpass $\dot{m}_{\text{min}} \cdot 1.5$ at start-up and triggers shut-down when falling below \dot{m}_{min} .

The number of panels n_{panel} and the number of tubes n_{tube} have a significant impact on the minimum mass flow rate. Thus, they play an important role in the receiver optimization, through affecting the amount of in-operation time. The power lost due to the receiver not being active is defined as

$$\dot{Q}_{\text{inactive}}^{(t)} = G_{\text{bn}}^{(t)} \cdot A_{\text{HSF}} \quad \forall t \text{ where } \dot{m}^{(t)} = 0 \quad (19)$$

2.2. Annual simulation with adaptive simulation model

The DPM described in Section 2.1 allows for transient simulation of the receiver integrated in the power plant system. However, this approach is not fast enough to be used for repeated annual simulations, as required for iterative optimization. Instead, an additional adaptive simulation model based on an Artificial Neural Network is introduced, which learns to reproduce the transient behavior of one specific receiver configuration. Training data is generated by simulating selected time ranges with the DPM. Eventually, an annual assessment is performed with the trained ANN. As the selected time ranges simulated with the DPM represent only a small fraction of the year, this approach is fast enough to be used in iterative optimization. In the following, the ANN setup, the training approach and the integration in the system model are described.

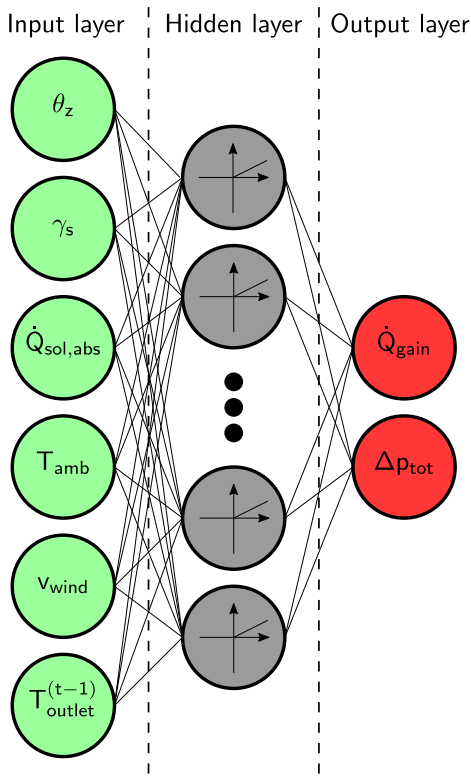


Fig. 6. ANN with input layer, one hidden layer with 100 *ReLU* neurons and output layer. Inputs are solar zenith angle θ_z , solar azimuth angle γ_s , absorbed solar radiation $\dot{Q}_{sol,abs}$, ambient temperature T_{amb} , wind speed v_{wind} and outlet temperature $T_{outlet}^{(t-1)}$ of the last time step. Outputs are power \dot{Q}_{gain} to the HTF and total pressure loss Δp_{tot} .

2.2.1. Artificial Neural Network model

The ANN is implemented with the *Python* library *Keras* (Chollet, 2015), using its backend *Theano* (Theano Development Team, 2016). The architecture of the ANN (see Fig. 6) consists of an input layer, one hidden layer with 100 neurons (which empirically proved to be a suitable number) and an output layer (Chollet, 2017). *Rectified Linear Units* (ReLU, Nair and Hinton, 2010) are used as activation functions in the hidden layer.

2.2.2. Training

To generate suitable data sets for the ANN training, the DPM is used to simulate a selection of characteristic days which represent a maximum variety of system states. In a pre-selection step, only days are considered, whose cumulative DNI is at least 50% of the maximum occurring daily cumulative DNI in the year. This rules out time periods where the system is not in operation at all. From the remaining time ranges, the following nine characteristic days are selected:

- Minimum, maximum and mean daily cumulative DNI
- Minimum, maximum and mean daily average wind speed
- Minimum, maximum and mean daily average ambient temperature

After normalizing the training data, the *Adam* optimizer (Kingma and Ba, 2014) is used with a learning rate of 0.001 and a decay rate of 0.001. Typically after 1000 training epochs, where 30% of the data is retained for validation, the model's residuals as represented by the *mean squared error* are converged.

2.2.3. Validation

For validation, the trained ANN model was compared to the results of a full year simulation with the DPM. The relative difference between

the two models in terms of $Q_{gain,an,th}$ is less than 0.1%. Likewise, the results from 10 training runs with the same input data have been evaluated, to guarantee that the statistical uncertainty of the training procedure is not significant. The maximum observed difference with respect to the mean value was equally less than 0.1%. While these deviations are small, they might have an impact on the calculation of a gradient, based on two consecutive evaluations of the objective function. This has to be considered in the selection of the optimization algorithm.

2.2.4. Integration in system simulation

An additional receiver model is implemented in *ColSim CSP*, which features the same interface as the DPM. Absorbed solar radiation is equally modeled using the *sky discretization* approach, but thermal losses are reproduced with the trained ANN. The trained ANN is integrated with the *ColSim CSP* code (C++) by means of the library *kerasify* (Rose, 2017).

2.3. Objective function and figure of merit

By integrating the ray tracing pre-calculations, the evaluation of the DPM for the characteristic days and the annual simulation with the ANN, an objective function is implemented as displayed in Fig. 3.

Nine free parameters describe one configuration of the receiver (see also Fig. 1) and are therefore DoFs to be optimized. They can be divided into three groups:

Geometry parameters

- Receiver width W_{rec}
- Receiver height H_{rec}
- Upper lip height H_{ul}
- Receiver inclination angle θ_{rec}

Hydraulic circuit parameters

- Number of panels n_{panel} , whose value has to be an integer multiple of 2, as the receiver will be operated with two parallel flow paths.
- Number of tubes per panel n_{tube} , whose value has to be an integer.

Aiming parameters

- Maximum horizontal aim point offset O_{hor}
- Maximum top vertical aim point offset $O_{vert,top}$
- Maximum bottom vertical aim point offset $O_{vert,bot}$

Further parameters (e.g. material properties) are out of scope for this study and are not considered as DoFs for the optimization. However, extension of the objective function with further DoFs is expected to be straightforward.

By evaluating the objective function, the effective annual thermal gain $Q_{gain,an,th}$ as a single figure of merit is calculated:

$$Q_{gain,eff,an} = \Delta t \cdot \sum_t (\dot{Q}_{gain}^{(t)} - \dot{Q}_{pump,th}^{(t)}) \quad (20)$$

with constant time step Δt .

2.4. Optimization algorithm

The principal choice regarding the optimization approach is between gradient-based hill-climbing algorithms – an optimum of the objective function is searched by following its slope where it is steepest – and gradient-free methods which usually apply some kind of meta-heuristic (Eiben and Smith, 2015). Several characteristics of the objective function are relevant for the selection of the optimization algorithm:

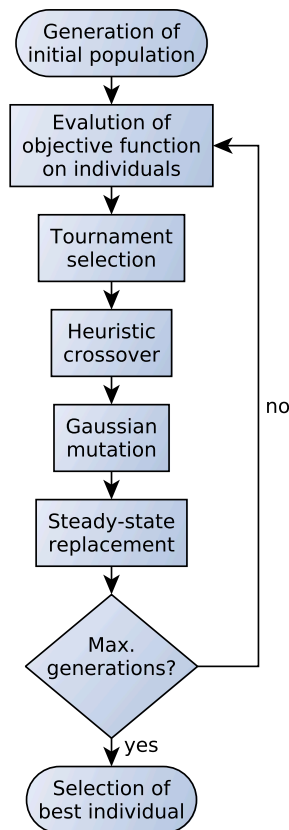


Fig. 7. Operators and flow graph of Evolutionary Algorithm.

- The objective function exhibits stochastic noise, i.e. two subsequent runs with the same input parameters might yield different results. This deteriorates the calculation of a gradient. The noise level is quantified in Appendix B.
- The objective function is not steady, as the *hydraulic circuit parameters* n_{panel} and n_{tube} have discrete integer values. This also complicates the calculation of a gradient.
- The objective function exhibits local maxima. As an example, two local maxima might be reached with two different numbers of panels and respectively suiting numbers of tubes per panel.
- The objective function has nine DoFs (problem size) and a single evaluation of the objective function takes time in the order of hours. Although there is no clear classification criterion, the computational effort can be considered high. The complexity of the numerical approximation of the objective function's gradient scales with the problem size and is therefore equally considered to be computationally intensive.

Based on these characteristics, *Evolutionary Algorithms* have been selected as optimization approach of choice (Eiben and Smith, 2015). The basic principle used herein (see also Fig. 7) consists of several steps:

1. Generate an initial population of random input parameter sets (within the search space) for the objective function. These candidate solutions are subsequently called *individuals*, their number is labeled *population size*.
2. Evaluate the objective function on each individual to determine its *fitness*, given by the effective annual thermal gain $Q_{\text{gain,an,th}}$ (see Section 2.3).
3. Select individuals from the *parent* population according to a method based on their performance.
4. Perform crossover of candidate solutions to generate *offspring* individuals.

5. Mutate the individuals' parameters according on a stochastic approach.
6. Select individuals for the *offspring* generation to replace the *parent* generation.
7. Repeat steps 2–5 until the maximum number of generations is reached.

As EAs do not require the calculation of the objective function gradient, they can deal well with noise. Furthermore, due to the initialization of the first population with random individuals within the search space and due to randomness introduced by the mutation operator, they are less prone to get stuck in local optima. EAs are well suited to converge to a good solution with reasonable computational effort, even for large problem sizes and computationally intensive objective functions (Eiben and Smith, 2015). This is supported by the inherent parallelism of EAs: the performance of each individual in a population can be evaluated independently of the other candidates.

To implement the EA, the Python library *inspyred* (Garrett, 2012) has been used. The components and the flow of the implemented EA are depicted in Fig. 7.

The theoretical foundation for the algorithmic setup is given by Eiben and Smith (2015): *tournament selection* is used to select individuals for crossover and mutation. With a tournament size of 2 and therefore a low selection pressure, the diversity of solutions is preserved to avoid premature convergence. The *meta-heuristic crossover* as implemented by *inspyred* is applied to mix selected individuals. The *mutation operator* is implemented with a Gaussian approach, having an individual standard deviation $\sigma_{\text{mut}} = 0.1 \cdot (b_{\text{max}} - b_{\text{min}})$ for each parameter, where b_{min} and b_{max} are the parameter's lower and upper bound respectively. *Steady-state replacement* is used to replace the least performing individuals from the old generation and guarantee a constant population size. *Elitism* is implemented such that 10 % of the parent generation are allowed to survive, if they have higher fitness than the weakest individuals in the offspring generation.

3. Application

The optimization methodology is exemplary applied to a polar HSF and a cavity receiver.

3.1. Optimization scenario

As a reference system for the cavity receiver optimization, the PS10 plant (Osuna et al., 2006) close to Seville, Spain has been selected. This choice is owing to the large amount of accessible information in literature. The PS10 receiver itself will not be compared with the optimization outcome, as it uses direct steam instead of molten salt as HTF, which entails different parameters regarding the receiver design.

Annual DNI values are obtained using the software *METEONORM* (METEOTEST, 2015). An exemplary value of 5% circumsolar ratio has been selected. While the sensitivity of this parameter has not been studied herein, it might have a significant impact on the optimized geometry of the receiver. Notably, lower circumsolar ratios are expected to entail smaller aperture dimensions. For a specific optimization at a given project site, a measured and thus locally representative circumsolar ratio should be used.

The heliostat positions are taken from Noone et al. (2012). Osuna et al. (2006) provide some data about the geometry of the tower. Due to a lack of detailed information, the tower trunk is simplified. Furthermore, the tower footprint is increased to allow for all possible receiver configurations to fit in. An optimization of the tower geometry is only reasonable in conjunction with an optimization of the HSF and therefore out of the scope of this study. All constant parameters of the optimization scenario with references are summarized in Table 1 and a visualization of the setup as implemented for ray tracing is depicted in Fig. 8.

Table 1

General parameters for the PS10 setup in Seville, Spain (Noone et al., 2012; Osuna et al., 2006). The sunshape is modeled according to Buie et al. (2003), optical absorber coating properties are considered for PYROMARK (Ho et al., 2012), tube wall thickness according to Rodríguez-Sánchez et al. (2014) and pump efficiency according to Rodríguez-Sánchez et al. (2014).

Site	
Latitude	37.43°N
Longitude	6.25°W
Elevation	63 m
Sun parameters	
Annual DNI	2348 kWh/m ²
Sunshape	Buie model
Circumsolar ratio	5%
Heliostats	
Tracking type	Azimuth-Elevation
Count	624
Surface shape	Single paraboloid facet, rectangular edges
Canting conditions	On-axis canting
Focal length	Slant range of heliostat
Width	12.84 m
Height	9.45 m
Facet reflectance	0.88
Beam quality	2.9 mrad
Field type	Polar north field
Receiver	
Heat Transfer Fluid	Molten salt
Design power $\dot{Q}_{sol,abs,design}$	55 MW _{th}
Solar absorptance	0.95
Longwave emittance	0.87
Tube wall thickness	1.65 mm
Tower	
Total height	120 m
Aperture center height H_{tower}	100.5 m
Footprint	rectangular: 18 m × 10 m
Power block	
Pump efficiency	0.7
Thermal-to-electric conversion efficiency	0.4

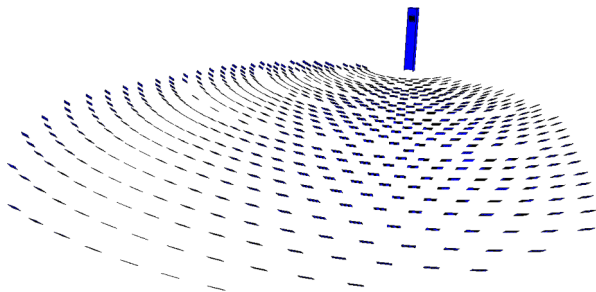


Fig. 8. Visualization of the PS10 optimization scenario including Heliostat Field, tower structure and exemplary configuration of the receiver, as implemented in the ray tracing setup.

Using the Fraunhofer ISE tool devISE_{CRS} (Jebamalai, 2016; Chaudhry, 2015), a reference parameter set for the receiver has been derived based on simplified design methods. This configuration’s fitness $Q_{gain,eff,an,ref}$ is subsequently used to benchmark the optimization progress. As the relative improvement equally depends on the optimized and reference configurations, this benchmark has to be treated with great caution. Table 2 presents the reference parameter set, along with upper and lower bounds that have been used in the optimization.

Table 2

Reference value, lower bound and upper bound for all free parameters of the objective function (see also Fig. 1)

Parameter	Lower b.	Reference	Upper b.
W_{rec}	6 m	9.23 m	14 m
H_{rec}	6 m	9.37 m	14 m
H_{ul}	0 m	0.94 m	4 m
θ_{rec}	0	17.26°	45°
n_{panel}	2	24	100
n_{tube}	1	25	100
O_{hor}	0 m	0 m	10 m
$O_{vert,top}$	0 m	0 m	7 m
$O_{vert,bot}$	0 m	0 m	7 m

3.2. Optimization results

The progress of the optimizations is displayed in Fig. 9. While the fitness of the initial population’s best candidate is yet below the value of the reference design, the candidate solutions improve quickly over the first few generations. In the later course of the optimization, the improvement gradient flattens. Finally, the population’s highest fitness converges towards a value, which is assumed to be close to the global optimum.

A comparison of the reference design and the best candidate solution at the end of the optimization in terms of a relative loss breakdown is displayed in Fig. 10. The ratio of $Q_{gain,eff,an}$ with respect to the potentially available energy on the HSF, $Q_{HSF,pot} = \sum_t G_{bn,t} \cdot A_{HSF} \cdot \Delta t$, rises from 52.1% to 54.3%. This represents a relative improvement of $Q_{gain,eff,an,opt}/Q_{gain,eff,an,ref} - 1 = 4.3\%$ compared to the reference.

The evolution of the candidates features is visualized in Fig. 11. Regarding the geometry parameters, the width and height of the optimized receiver ($W_{rec,opt} = 9.84$ m, $H_{rec,opt} = 9.87$ m) increase with respect to the reference design. Even if this implies a receiver with larger absorber panels, the optimized upper lip covers about 14% of the aperture ($H_{ul,opt} = 1.38$ m) and consequently optical losses $Q_{loss,sol,an}$ are increased as compared to the reference. Due to more exposed surface area and higher surface temperatures (see hydraulic circuit parameters), thermal losses $Q_{loss,th,an}$ are also higher. While the increase of both optical and thermal losses is surprising at first glance, the optimized receiver configuration represents the ideal trade-off with respect to at the same time strongly reduced inactivity losses $Q_{inactive,an}$ (see Fig. 10). For comparison, a single evaluation of the objective function has been carried out, based on the optimized receiver configuration, but with $H_{ul} = 0$. While $Q_{loss,sol,an}$ is reduced as compared to the configuration with $H_{ul,opt} = 1.38$ m, the resulting $Q_{gain,eff,an}$ is 0.7% lower than $Q_{gain,eff,an,opt}$ due to higher thermal losses. As mentioned in Section 3.1, a lower circumsolar ratio might reduce the dimensions of the optimized aperture opening.

The optimized cavity inclination ($\theta_{rec,opt} = 10.5^\circ$) is slightly smaller than the reference value. This suggests that – while the simplified design approach orienting the cavity towards the mean vision ray of the HSF is already quite efficient – the optimized projection of the cavity aperture favors heliostats further away. This is reasonable, as heliostats with a large slant range have a large focal spot. Therefore, increasing the projected cavity aperture area for these heliostats will decrease their spillage.

The optimized hydraulic circuit parameters ($n_{panel,opt} = 70$, $n_{tube,opt} = 4$) differ very significantly from the reference. The number of panels is more than twice higher than the reference ($n_{panel,ref} = 24$) and the number of tubes per panel is significantly lower ($n_{tube,ref} = 25$). Defining the hydraulic circuit parameters (together with the receiver width W_{rec}) also determines the inner diameter of the

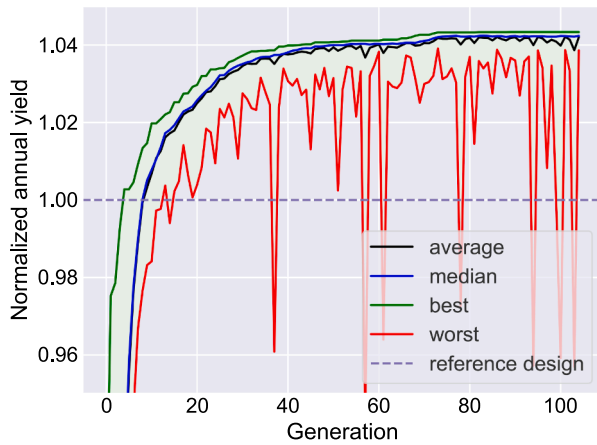


Fig. 9. Optimization progress in terms of the effective annual thermal gain normalized with the reference value, $Q_{\text{gain,eff,an,opt}}/Q_{\text{gain,eff,an,ref}}$. The figure shows each generation's best, worst, median and average candidate solutions over the course of the optimization.

absorber tubes d_{in} . Therefore, the optimum arrangement entails absorber tubes with increased inner diameter ($d_{\text{in,opt}} = 5.2 \text{ cm}$) as compared to the reference ($d_{\text{in,ref}} = 2.1 \text{ cm}$). The maximum occurring mass flow rates observed during the simulation implies flow velocities of 4.5 m/s and 4.2 m/s for the reference and optimized receiver configuration respectively. These values are close to the recommendation of 4 m/s by Tilley et al. (2014). Annually, the average pressure drop and the surface temperatures are slightly increased while the minimum

mass flow rate is significantly reduced. As a consequence, the losses $Q_{\text{inactive,an}}$ due to the receiver not being active are significantly smaller, while thermal losses $Q_{\text{loss,th,an}}$ are higher. In the simplified design routine as applied for the reference, the operational aspects are not taken into consideration, which leads to these significant deviations of the optimized receiver configuration regarding the hydraulic circuit parameters. Discussions with CSP industry have revealed that a very large number of panels – while being technically feasible – would entail very high receiver costs. Thus, in practise, $n_{\text{panel,opt}} = 70$ would be too expensive. It is expected that integration of economic aspects and cost functions in the objective function would lead to significantly different optimum hydraulic circuit parameters. This remains subject to future work.

The maximum offset values of the aiming parameters converge against different, yet stable values during the course of the optimization ($O_{\text{hor,opt}} = 0.30 \text{ m}$, $O_{\text{vert,top,opt}} = 0.49 \text{ m}$, $O_{\text{vert,bot,opt}} = 0.007 \text{ m} \approx 0 \text{ m}$). This demonstrates that the optimizer is able to reduce the thermal losses through homogenizing the flux distribution, while not significantly increasing the optical losses. With the aiming strategy and the optimized maximum vertical offsets, heliostats far away are focused at the aperture center, while heliostats close to the tower aim at higher regions. This is reasonable, as heliostats with a short slant range exhibit a small focal spot at the receiver. Therefore, they can efficiently irradiate the upper parts of the absorber panels, without being blocked by the upper lip. Consequently, the maximum top vertical aim point offset can be larger than its bottom equivalent ($O_{\text{vert,top,opt}} > O_{\text{vert,bot,opt}}$).

For the optimized receiver, Fig. 12 displays exemplary distributions of HTF bulk, HTF film and absorber surface temperature, as well as radiation concentration on the absorber panels. Due to the solar noon

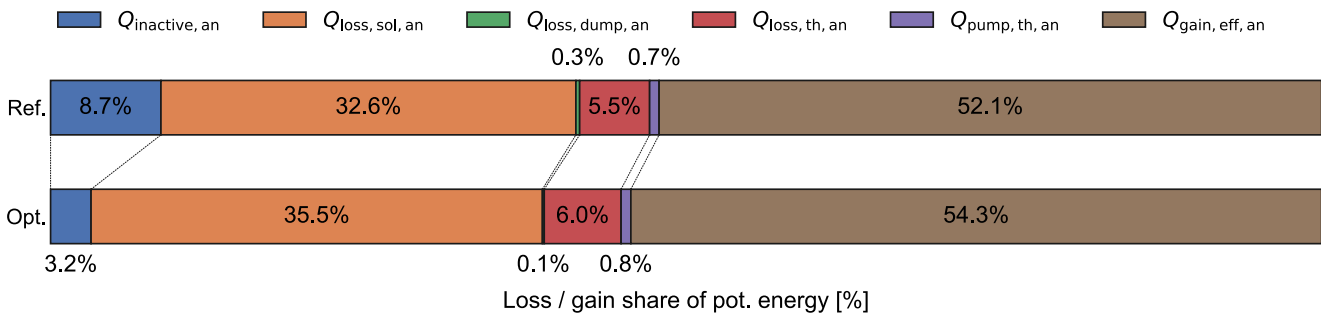


Fig. 10. Break-down of annual losses (annual loss $Q_{\text{inactive,an}} = \sum_t \dot{Q}_{\text{inactive}}^{(t)} \Delta t$ due to the receiver being inactive, annual solar optical loss $Q_{\text{loss,sol,an}} = \sum_t \dot{Q}_{\text{loss,sol}}^{(t)} \Delta t$, annual dumping loss $Q_{\text{loss,dump,an}} = \sum_t \dot{Q}_{\text{loss,dump}}^{(t)} \Delta t$, annual thermal loss $Q_{\text{loss,th,an}} = \sum_t \dot{Q}_{\text{loss,th}}^{(t)} \Delta t$ and annual equivalent thermal pumping energy $Q_{\text{pump,th,an}} = \sum_t \dot{Q}_{\text{pump,th}}^{(t)} \Delta t$) and effective annual thermal gain ($Q_{\text{gain,eff,an}}$) for the reference and optimized candidates, represented as shares of the potentially available energy $Q_{\text{HSF,pot}} = \sum_t G_{\text{bn}}^{(t)} \cdot A_{\text{HSF}} \cdot \Delta t$.

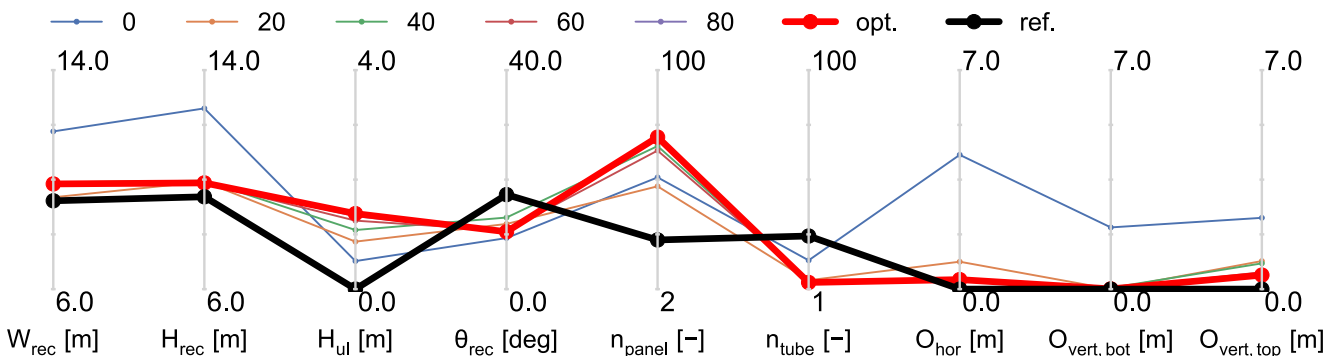


Fig. 11. Feature evolution within the boundaries, for the best candidates in the population. Reference and optimized configurations are represented with bold black and red lines respectively, the other colors depict the initial generation of the optimization and some intermediates. (For interpretation of the references to colour in this figure legend, the reader is referred to the web version of this article.)

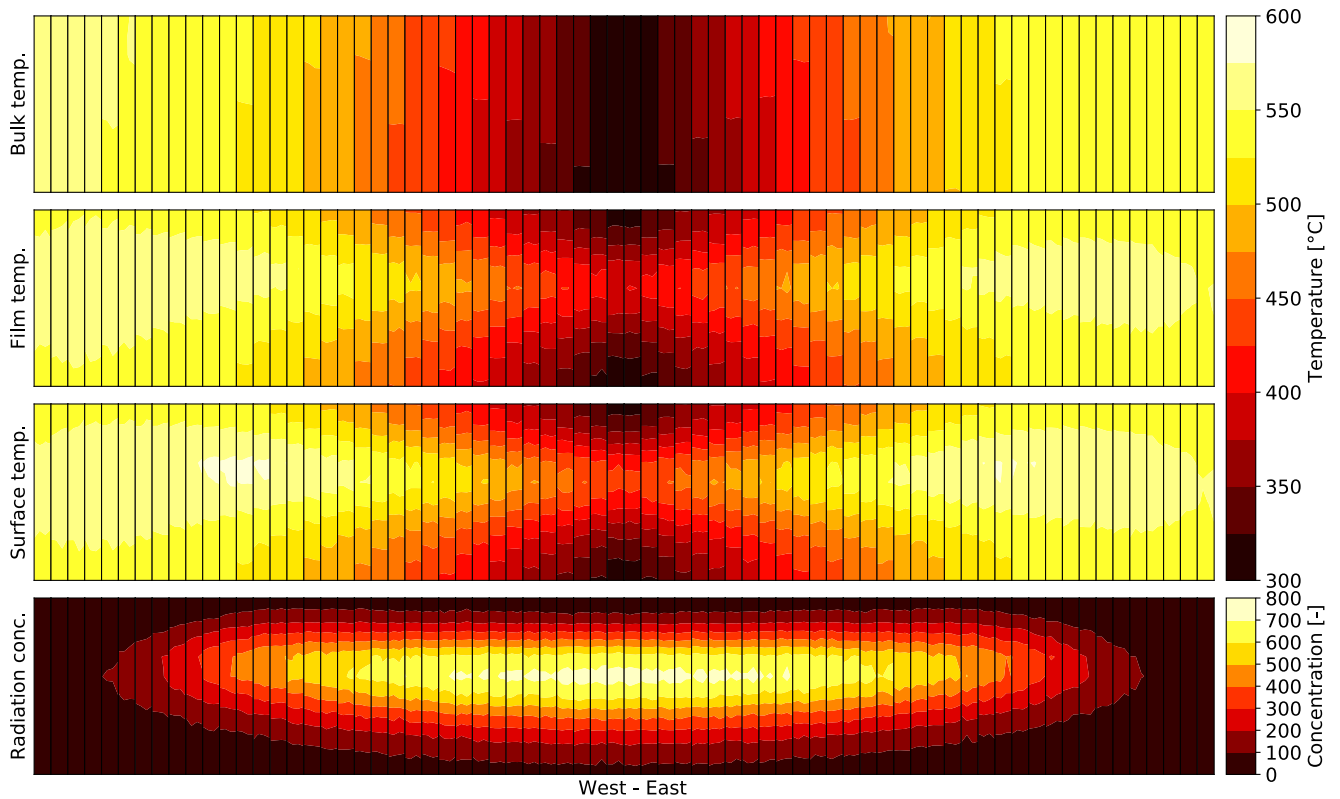


Fig. 12. Distributions of HTF bulk temperature T_{HTF} (max. value: 551 °C), HTF film temperature T_{film} (max. value: 565 °C) and absorber surface temperature T_{surf} (max. value: 580 °C) and radiation concentration (max. value: 764) on absorber panels (left/west - right/east), for the optimized receiver configuration on Sep 3 close to solar noon with $G_{bn} = 637 \text{ W/m}^2$.

sun position, the radiation distribution – and consequently also the temperature distributions – is very symmetric on the panels. The bulk temperature distribution visualizes the flow pattern as introduced in Fig. 2, with temperature increasing from the center panels outwards and from the panels’ bottom to the top. With the radiation concentration being highest on the central absorber areas, the bulk temperature increase along the fluid flow in the outermost panels is low. The film and surface temperatures originate from the bulk temperature as a baseline and from a temperature increase roughly proportional to the radiation concentration (see also Section 2.1.4). From the DPM simulations for all characteristic days, a maximum film temperature of 628.5°C is observed. This is below the critical value of 630°C, as given by Rodríguez-Sánchez et al. (2014) regarding molten salt corrosivity. However, the value could be significantly reduced by dynamically adapting the mass flow ratio between both flow branches, according to the sun position and the resulting east/west radiation distribution on the absorber panels. This might further reduce the thermal losses and remains subject for future work.

For the optimized receiver geometry, the simulation has been repeated without aiming offsets (single aim point in the aperture center). For the same time instant as displayed in Fig. 12, this increases the maximum radiation concentration from 764 suns to 856 suns. Annually, $Q_{gain,eff,an}$ is decreased by 0.03% as compared to the optimized configuration with non-zero aiming offsets. While the benefit on the effective annual thermal gain due to aiming strategy is rather small, the maximum occurring film temperature is increased to 633°C. This suggests that a single aim point approach performs reasonably well, as long as no further constraints regarding maximum radiation concentration are considered.

While a detailed cost assessment is out of the scope of this study, it is assumed that – apart from the larger number of panels – the cost of the optimized receiver is not significantly different as compared to the reference configuration. Under these circumstances, a relative increase of 4.3% in effective annual gain would represent an important improvement for a commercial system, that could be achieved during the conceptual stage of a CRS plant.

3.3. Computational performance

For the presented case study, 32 CPU cores (AMD Opteron™ Processor 6378, 2.4 GHz) were used for parallelizing the objective function evaluation for different individuals of each generation’s population. On a single core, the evaluation of the objective function took about 3000 s, with the solar radiation ray tracing ($\approx 67\%$) and the DPM simulations for characteristic days ($\approx 26\%$) being the main time consumers. This resulted in an overall optimization duration of about 10 d.

With more computational resources, extended parallelization – and thus reduced optimization duration – would be possible. The solar radiation assessment is independent for different sky nodes and consequently readily parallelized, as are the DPM simulations for different characteristic days. Furthermore, both the ray tracing (solar radiation, view factors) and the ANN training are inherently parallel.

3.4. Range of applicability

Within the scope of this study, the application of the developed optimization methodology is demonstrated for a small-scale cavity

system, in contrast to current commercial plants. However, most of the methodology components are not limited to this type of system. In the following, limitations of the methodology and the potential range of applicability are briefly discussed, theoretically covering scenarios that were not studied herein.

The transient optical modeling can be applied to all kinds of CRS with receivers based on non-volumetric surface absorbers. The detailed thermo-hydraulic receiver model in its current form is able to simulate various tube-panel-based receiver configurations and the black-box ANN model can use training data from any source. Apart from parameter bounds, the optimization algorithm doesn't need further information about the objective function. Therefore, the latter can be readily extended with further parameters or models.

This evidences that the presented optimization methodology can be applied – potentially with modifications – to different CRS, like:

- surround heliostat fields with external receivers (demonstrated within this study for the *Solar Two* system, see [Appendix A](#))
- large, commercial systems in the range of 100 MW_{el} (larger numbers of heliostats and receiver tubes might lead to higher computational costs which could be tackled with stronger simulation hardware and increased parallelization.)
- direct steam systems
- novel receiver technologies with different HTF for higher operating temperatures
- multi-tower arrangements

While being out of the scope of this study, the optimization objective function could be broadened, such that e.g. HSF, storage system and power block are included. As discussed above, applicability to commercial systems will require to include cost considerations in the figure of merit.

With the concrete aim of optimizing a receiver based on a given technology and with defined boundary conditions, a thorougher uncertainty analysis of the simulation model and more extensive validations with appropriate measurement data should be performed.

4. Conclusion

A receiver optimization methodology has been presented, which is based on a detailed transient optical and thermo-hydraulic receiver model. It covers all relevant energy conversion mechanisms from solar radiation to thermal energy in the HTF and includes electricity generation in a simplified manner. The *Detailed Physical Model* is partly validated with experimental data from the *Solar Two* project. To be able to use *annual* thermal gain as a figure of merit in the iterative optimization, an adaptive *Artificial Neural Network* trained with data from the detailed model and a sky discretization approach accelerate the evaluation. An *Evolutionary Algorithm* is applied to find the global optimum for a receiver configuration with nine free parameters, covering its geometry, hydraulic circuit and aiming strategy. Contrary to gradient-based optimizers, *Evolutionary Algorithms* can deal well with the noisy

Appendix A. Comparison and validation with data from the *Solar Two* project

For validation of the DPM, simulation results are compared to measurement data obtained from the *Solar Two* project ([Pacheco et al., 2002](#)), a CRS with an external molten salt receiver and a surround field. The *Solar Two* system is only partly suited for comparison, as it did not include a cavity. Thus, due to the lack of alternative experimental data, only some aspects of the DPM model can be compared:

- Thermo-hydraulic tube model
- Molten salt as HTF
- Transient solar radiation model on the receiver panels
- Radiative heat transfer between neighboring tubes

objective function as used in this study, are less prone to run into local optima and are able to identify an optimum receiver configuration within reasonable time.

Being applied to a small-scale molten salt cavity receiver system (similar to PS10), the methodology allows to increase the annual yield of the optimized receiver configuration by 4.3% compared to a reference solution derived with a conventional design point approach. The largest differences between optimized and reference solutions occur for the *hydraulic circuit parameters*. As their impact only becomes evident by using transient analysis, the importance of annual system assessment is highlighted. A sensitivity analysis performed for the optimum solution shows that deviations from the optimum *geometry parameters* have the strongest impact on the figure of merit, followed by the *hydraulic circuit parameters* and the *aiming parameters*.

A discussion of the methodology's range of applicability highlights that most constituents of the tool chain could be readily adapted to setups beyond polar fields and molten salt cavities. Thus, the methodology is expected to be applicable for the assessment and optimization of various receiver technologies and tower systems. In particular, large-scale surround field CRS as currently built in commercial projects could be covered.

4.1. Outlook

As part of future work, several aspects of the detailed simulation model could be improved: among them are a more accurate representation of convective losses, introduction of a dynamically adapting flow pattern and more detailed models for the other components of the CRS. Furthermore, the presented methodology to optimize receivers could be extended towards a more holistic system optimization (including Heliostat Field design and storage system / power block dimensioning) and taking into account costs. In terms of the optimization, the operators of the EA could be dynamically adapted over the iterations, to accelerate the algorithm's convergence.

Declaration of Competing Interest

None.

Acknowledgments

The work presented in this paper has been partly conducted within the project *HelioPack*, which was funded by the German Federal Ministry for Economic Affairs and Energy (BMWi) under grant 0325659A, and the project *POLYPHEM*, which is funded by the *European Commission* under grant 764048. The authors of this publication are responsible for its contents.

The authors would like to acknowledge the helpful feedback from Prof. Dr. Aldo Steinfeld. Furthermore, the preliminary studies of Florian Kiefer, Jonathan Flesch, Talal Chaudhry and Joseph S. Maria Jebamalai in the scope of their Master theses are gratefully acknowledged.

Aspects, which can not be compared, are:

- Thermal radiation transport in a cavity
- Convective heat transfer in a cavity under wind influence
- Pressure losses (not included in the measurement data)

The validation procedure is very similar as described by [Fritsch et al. \(2017\)](#). Thus, the following description only highlights the main concept and differences.

A.1. Description of Solar Two data

The Solar Two receiver measurement campaign consisted of nine days. As no means were available to directly measure the thermal losses of the receiver, an indirect approach via assessing the power to the HTF was suggested by [Pacheco et al. \(2002\)](#). For each day, four measurement periods around solar noon were carried out: two periods with all available heliostats focused on the receiver (*full power*) and two periods with only half of the available heliostats on target (*half power*). This allowed to set up an heat balance equation system, from which the unknown absorbed power on the receiver can be eliminated and a single value for the thermal losses $\dot{Q}_{\text{loss,th}}$ is obtained for each measurement day.

An important assumption is made: “Under steady-state conditions with constant inlet and outlet salt temperatures and wind velocities, the temperature distributions on the receiver surface and throughout the receiver are independent of power level. Therefore, the thermal losses [...] are independent of the incident power ([Pacheco et al., 2002, p.110](#))”. This can only be seen as an approximation, as the surface temperatures would be higher for full-load conditions. Due to the method, with which the receiver efficiency was determined, the measurements can inherently not represent dependencies of the absorbed power, therefore also excluding mass flow rate, number of heliostats tracking the receiver and DNI. The measurement equipment introduced further uncertainties ([Pacheco et al., 2002](#)).

A.2. Modeling of Solar Two

The modeling procedure is similar to the approach described by [Fritsch et al. \(2017\)](#). The Solar Two system has been modeled according to the description in [Pacheco et al. \(2002\)](#). The solar field contains both *Lugo* and *Martin-Marietta* heliostats. A visualization as implemented for ray tracing is depicted in [Fig. 13](#). The 24 panels of the Solar Two receiver were arranged with two flow paths and meandering upwards-downwards flow from panel to panel. The operating conditions during the measurements (mass flow rate, inlet temperature) were reproduced as closely as possible. Furthermore, environmental conditions (wind speed, DNI, ambient temperature) were configured according to the published data. Convective heat transfer coefficients were calculated according to [Siebers and Kraabel \(1984\)](#), where wind direction is neglected. The radiation distribution maps on the receiver surfaces are scaled such that – for the given DNI and mass flow rates – the measured outlet temperature is reached ([Fritsch et al., 2017](#)). The scaling is performed with the flux map interpolation method as published by [Schöttl et al. \(2018\)](#).

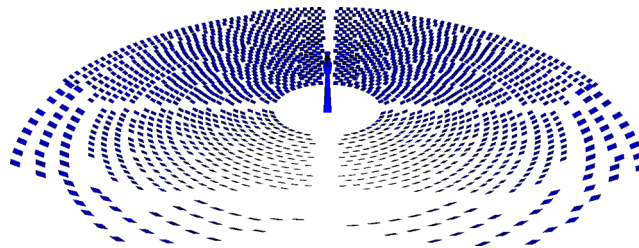


Fig. 13. Visualization of the Solar Two setup including HSF, tower structure and receiver, as implemented in the ray tracing setup.

A.3. Solar Two comparison results and discussion

[Fig. 14](#) shows a comparison between simulated thermal losses and measurement results published by [Pacheco et al. \(2002\)](#). Relative deviations are calculated as

$$\Delta \dot{Q}_{\text{loss,th,meas}} = \dot{Q}_{\text{loss,th,sim,avg}} / \dot{Q}_{\text{loss,th,meas}} - 1 \quad (21)$$

where an average value of all four simulated $\dot{Q}_{\text{loss,th,sim}}$ of one measurement day is used.

Two trends are clearly visible from the simulated data: (a) the thermal losses rise for increasing wind speed and (b) for the same wind speed, thermal losses are higher for the *full power* than for the *half power* scenarios. Trend (a) can be attributed to stronger forced convection losses. Trend (b) is explained by increased convective and radiative losses, due to higher absorbed flux and accordingly higher surface temperatures for the *full power* scenarios.

[Pacheco et al. \(2002\)](#) calculated the uncertainty level on the receiver efficiency based on the estimated measurement uncertainty of the instruments (see [Fig. 14](#) center). From this, the respective uncertainty levels for the thermal losses are derived ([Pacheco et al., 2002, p.110, equation B-10](#)). The calculation methodology for the measured thermal losses is itself based on several assumptions and therefore introduces additional uncertainties that are not included here.

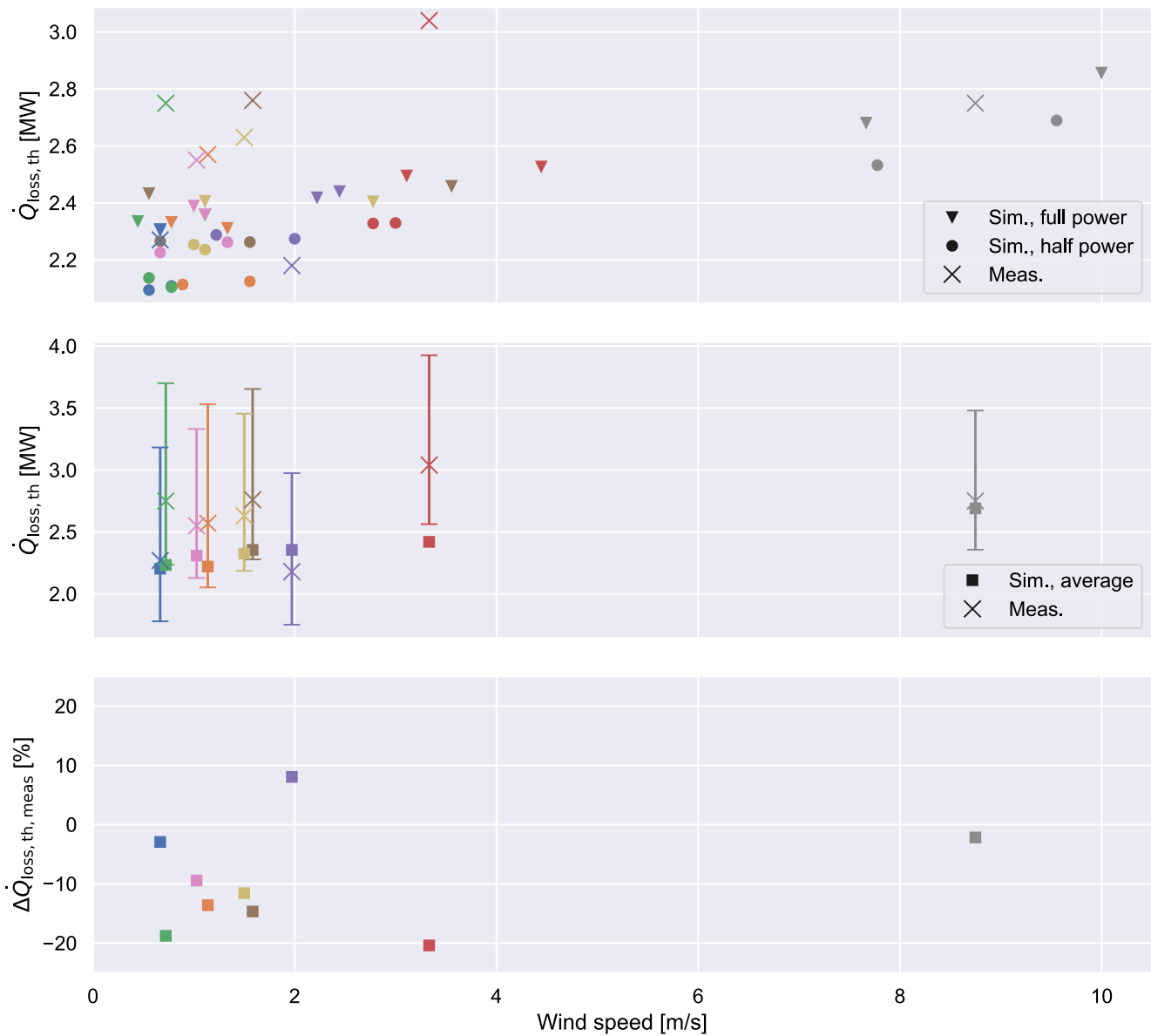


Fig. 14. Top: for each day of the measurement campaign, thermal losses $\dot{Q}_{\text{loss,th}}$ as a function of wind speed, from DPM simulations (two for full power and two for half power) and from measurement results published by Pacheco et al. (2002) (one average value). Center: comparison of the averaged results from the DPM simulations and the measurement results, including uncertainty levels. Bottom: relative deviations $\Delta\dot{Q}_{\text{loss,th,meas}}$ of simulations and measurements. Color coding is used to show which data points belong to the same measurement day.

Given the high uncertainty of the measurement results, the agreement of the outcome from simulation and measurement can be considered good. The highest relative deviation of 20.4% is observed for a medium wind speed day (red data points). As the respective measurement result lies far outside of the expected trend line regarding the wind speed dependency, Fritsch et al. (2017) suspect a measurement error. Overall, the DPM seems to slightly underpredict the thermal losses as compared to the measurements. Pacheco et al. (2002) mention 300 kW of additional convective losses from the gap between the back of the Solar Two receiver panels and the insulation. These are not modeled in the DPM, but would – if considered – contribute to match the simulation and measurement results better. As discussed in Section 2.1.4, heat losses through the back side are assumed to be negligible for modern molten salt receivers.

In addition, Fig. 15 shows a comparison between simulated thermal losses from the DPM and from the model by Fritsch et al. (2017) for all three days, for which results were given in Fritsch et al. (2017). Based on the published mass flow rates used in Fritsch et al. (2017), all three data points can be considered *full power* scenarios. Relative deviations $\Delta\dot{Q}_{\text{loss,th,Fritsch}}$ are calculated equivalently to Eq. 21.

The same trend regarding the wind speed dependency as in Fig. 14 is again visible. Results from both simulations models match well, with relative deviations below 5%. As compared to the Fritsch et al. (2017) model, the DPM seems to predict slightly higher losses for low wind conditions and slightly lower losses for stronger wind speeds.

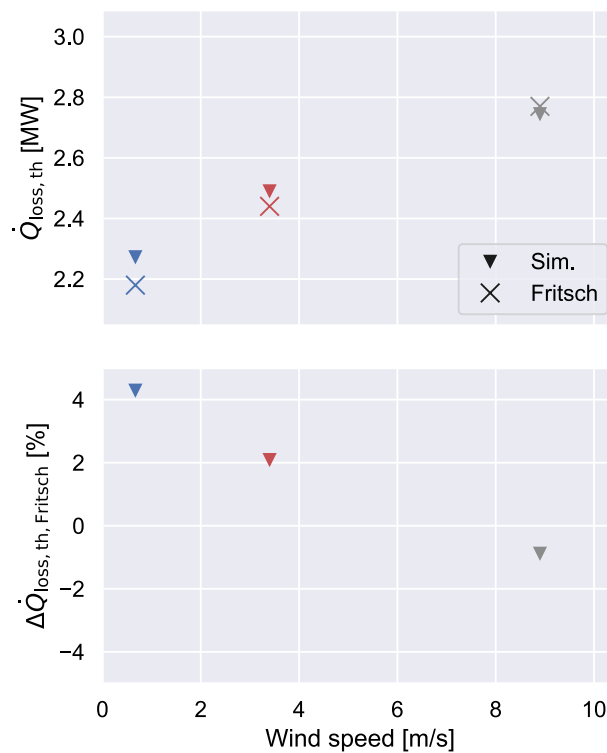


Fig. 15. Top: simulated thermal losses $Q_{loss,th}$ as a function of wind speed, from the DPM and from the model by Fritsch et al. (2017), who gave results for three days of the Solar Two measurement campaign. Bottom: relative deviations $\Delta Q_{loss,th, Fritsch}$ of both simulation models. The same color coding as in Fig. 14 is used to underline the affiliation of data points and measurement days. (For interpretation of the references to colour in this figure legend, the reader is referred to the web version of this article.)

Appendix B. Sensitivity analysis for the optimized receiver configuration

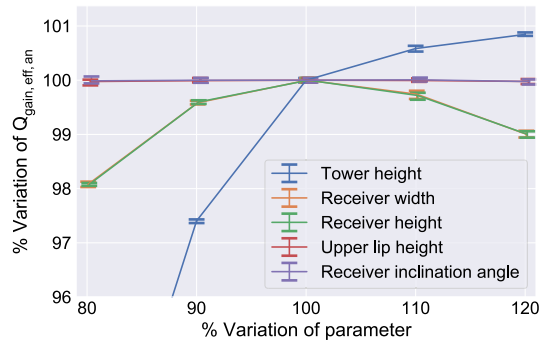
With optimization results at hand, a sensitivity analysis has been carried out, to study the parameters’ behavior and gradient close to the optimum design. Due to the lack of cost considerations in the objective function and due to the heliostat field not being optimized simultaneously, the tower height had not been included in the optimization. It is however studied within the sensitivity analysis, to investigate its impact in comparison to the other parameters. As only one parameter has been varied at a time, with all others set to the optimum value, dependencies between the parameters cannot be depicted by this analysis. To quantitatively investigate the uncertainty as introduced in Section 2.2.3, the entire sensitivity analysis has been carried out 20 times.

The results are depicted in Figs. B.16a, b and c for *geometry parameters*, *hydraulic circuit parameters* and *aiming parameters* respectively. The minimum and maximum values obtained from 20 evaluations of the objective function for each studied configuration are displayed as the lower and upper ends of an error bar respectively, while the data point itself is the mean value.

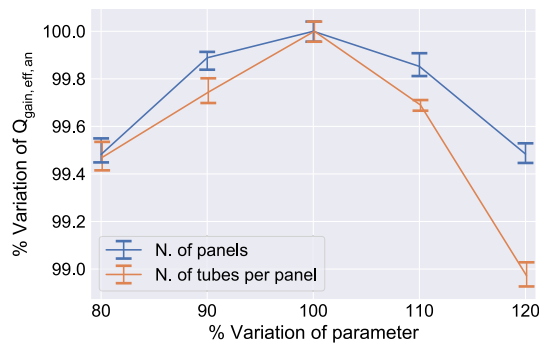
The *geometry parameters* have a strong impact on the effective annual thermal gain $Q_{gain,eff,an}$. It increases with rising tower height due to an improved optical efficiency. As the heliostat field and the distances between heliostat rows were designed for the reference tower height, reducing it results in a strong reduction of $Q_{gain,eff,an}$ due to additional blocking losses. Increasing the tower height has a much smaller effect in comparison. Changes in receiver width and receiver height result in an almost identical decrease of $Q_{gain,eff,an}$. Sensitivity with regard to the height of the upper lip is significantly smaller, which indicates that the trade-off between optical and thermal losses follows a flat profile around the optimum. It is important to note that there is a strong intercorrelation between the cavity aperture size (W_{rec} , H_{rec} , H_{ul}) and the *aiming parameters*, which is not depicted by the sensitivity analysis. Changes of the receiver inclination result in different receiver aperture projections for the heliostats, which implies a cosine-shaped trend of $Q_{gain,eff,an}$ in the neighborhood the optimum configuration. As the cosine is close to unity for small angles, the dependency of the effective annual thermal gain on the receiver inclination is very weak.

The influence of the *hydraulic circuit parameters* is lower as for the *geometry parameters* (different scale in Fig. 16b). Deviations of both number of panels and number of tubes per panel from their respective optimum values result in a clear decrease of effective annual thermal gain.

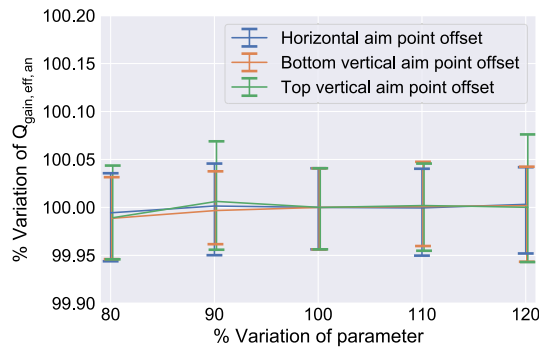
The impact of small changes of the *aiming parameters* on $Q_{gain,eff,an}$ is more than an order of magnitude smaller than the uncertainty resulting from stochastic effects in the objective function. Therefore, no meaningful conclusions can be drawn regarding the sensitivity of the *aiming parameters*. However, Fig. 16c highlights that the optimization routine must be able to deal with the noise of the objective function.



(a) Geometry parameters: tower height, cavity height, cavity width, upper lip height, cavity inclination



(b) Hydraulic circuit parameters: number of panels, number of tubes per panel



(c) Aiming parameters: horizontal aim point offset, top vertical aim point offset, bottom vertical aim point offset

Fig. 16. Results of sensitivity analysis: dependency of objective function (normalized with optimum design fitness) on variation of parameters in vicinity of the optimum design. For better visualization, a small horizontal offset has been introduced between data points with equal abscissa values to avoid overlapping of the error bars.

References

Asselineau, C.-A., Zapata, J., Pye, J., 2015. Geometrical shape optimization of a cavity receiver using coupled radiative and hydrodynamic modeling. *Energy Proc.* 69, 279–288.

Augsburger, G., 2013. Thermo-economic optimisation of large solar tower power plants. Ph.D. thesis, École Polytechnique Fédérale de Lausanne.

Augsburger, G., Das, A.K., Boschek, E., Clark, M.M., 2016. Thermo-mechanical and optical optimization of the molten salt receiver for a given heliostat field. In: AIP

Conference Proceedings 1734. AIP Publishing, Melville, New York, p. 030005.

Benoit, H., Spreafico, L., Gauthier, D., Flamant, G., 2016. Review of heat transfer fluids in tube-receivers used in concentrating solar thermal systems: properties and heat transfer coefficients. *Renew. Sustain. Energy Rev.* 55, 298–315.

Branke, R., Heimsath, A., 2010. Raytrace3D-Power Tower - A Novel Optical Model For Central Receiver Systems. In: *SolarPACES 2010, 16th Solar Power And Chemical Energy Systems International Symposium*, September 21–24. PSE.

Buie, D., Monger, A.G., Dey, C.J., 2003. Sunshape distributions for terrestrial solar simulations. *Sol. Energy* 74 (2), 113–122.

Carrizosa, E., Domínguez-Bravo, C., Fernández-Cara, E., Quero, M., 2015. Optimization of

- multiple receivers solar power tower systems. *Energy* 90, 2085–2093.
- Chaudhry, T.M., 2015. Development of a Program for Fast Design of Solar Tower Power Plants. Master's thesis, University of Stuttgart, High Performance Computing Center Stuttgart and Fraunhofer. Institute for Solar Energy Systems ISE.
- Chollet, F., 2015. Keras. <<https://github.com/fchollet/keras>>.
- Chollet, F., 2017. Deep Learning with Python. Manning Publications Company.
- Clausing, A.M., 1983. Convective losses from cavity solar receivers—comparisons between analytical predictions and experimental results. *J. Sol. Energy Eng.* 105 (1), 29.
- Craig, K.J., Gauché, P., Kretschmar, H., 2014. Optimization of solar tower hybrid pressurized air receiver using CFD and mathematical optimization. *Energy Proc.* 49, 324–333.
- Eiben, A.E., Smith, J.E., 2015. Introduction to Evolutionary Computing, second ed. Springer Publishing Company, Incorporated.
- Flesch, R., Högemann, D., Hackmann, J., Uhlig, R., Schwarzbözl, P., Augsburg, G., Clark, M., 2017. Dynamic modeling of molten salt power towers. *AIP Conf. Proc.* 1850 (1), 030016.
- Fritsch, A., Uhlig, R., Marocco, L., Frantz, C., Flesch, R., Hoffschmidt, B., 2017. A comparison between transient CFD and FEM simulations of solar central receiver tubes using molten salt and liquid metals. *Sol. Energy* 155, 259–266.
- Garrett, A.L., 2012. inspyred: Bio-inspired Algorithms in Python. URL <<http://aarongarrett.github.io/inspyred/>>.
- Heimsath, A., Bern, G., van Rooyen, D., Nitz, P., 2014. Quantifying optical loss factors of small linear concentrating collectors for process heat application. *Energy Proc.* 48, 77–86.
- Ho, C.K., Mahoney, A.R., Ambrosini, A., Bencomo, M., Hall, A., Lambert, T.N., 2012. Characterization of Pyromark 2500 Paint for High-Temperature Solar Receivers. In: Proceedings of ASME 2012 6th International Conference on Energy Sustainability & 10th Fuel Cell Science. Vol. 136. p. 014502.
- Jebamalai, J.S.M., 2016. Receiver Design Methodology for Solar Tower Power Plants. Master's thesis. KTH Royal Institute of Technology.
- Kiefer, F., 2013. Modelling and Simulation of a Cavity-Type Solar Thermal Central Receiver System. Master's thesis. Technische Universität München.
- Kim, J., Kim, J.-S., Stein, W., 2015. Simplified heat loss model for central tower solar receiver. *Sol. Energy* 116, 314–322.
- Kingma, D.P., Ba, J., 2014. Adam: A Method for Stochastic Optimization. CoRR abs/1412.6980.
- Kolb, G.J., Ho, C.K., Mancini, T.R., Gary, J.A., 2011. Power Tower Technology Roadmap and Cost Reduction Plan. Tech. Rep. SAND2011-2419, Sandia National Laboratories, Albuquerque, NM. <<http://prod.sandia.gov/techlib/access-control.cgi/2011/112419.pdf>>.
- METEOTEST, 2015. Meteotest Handbook Part I: Software (Version 7.1/ July 2015). <http://meteotest.com/images/uploads/downloads/mn71_software.pdf>.
- Nair, V., Hinton, G.E., 2010. Rectified Linear Units Improve Restricted Boltzmann Machines. In: Proceedings of the 27th International Conference on Machine Learning (ICML-10). pp. 807–814.
- Noone, C.J., Torrilhon, M., Mitsos, A., 2012. Heliostat field optimization: a new computationally efficient model and biomimetic layout. *Sol. Energy* 86 (2), 792–803.
- Osuna, R., Olavarría, R., Morillo, R., Sánchez, M., Cantero, F., Fernández-Quero, V., Robles, P., López del Cerro, T., Esteban, A., Cerón, F., Talegón, J., Romero, M., Téllez, F., Marcos, M.S., Martínez, D., Valverde, A., Monterreal, R., Pitz-Paal, R., Brakmann, G., Ruiz, V., Silva, M., Mennai, P., 2006. PS10, construction of a 11MW solar thermal power plant in Seville, Spain. In: SolarPACES 2006, 13th Solar Power And Chemical Energy Systems International Symposium.
- Pacheco, J.E., Bradshaw, R.W., Dawson, D.B., de La Rosa, W., Gilbert, R., Goods, S.H., Hale, M.J., Jacobs, P., Jones, S.A., Kolb, G.J., Prairie, M.R., Reilly, H.E., Showalter, S.K., Vant-Hull, L.L., 2002. Final Test and Evaluation Results from the Solar Two Project. Tech. Rep. SAND2002-0120, 793226, Sandia National Laboratories, Albuquerque, NM (United States). <<http://www.osti.gov/servlets/purl/793226-0lbooq/native/>>.
- Ramos, A., Ramos, F., 2012. Strategies in tower solar power plant optimization. *Sol. Energy* 86 (9), 2536–2548.
- Rodríguez-Sánchez, M.R., Sanchez-Gonzalez, A., Marugan-Cruz, C., Santana, D., 2014. Saving assessment using the PERS in solar power towers. *Energy Convers. Manage.* 87, 810–819.
- Rodríguez-Sánchez, M.R., Soria-Verdugo, A., Almendros-Ibáñez, J.A., Acosta-Iborra, A., Santana, D., 2014. Thermal design guidelines of solar power towers. *Appl. Therm. Eng.* 63 (1), 428–438.
- Rose, R., 2017. kerasify. URL <<https://github.com/moof2k/kerasify>>.
- Schöttl, P., Bern, G., van Rooyen, D., Flesch, J., Fluri, T., Nitz, P., 2018. Efficient modeling of variable solar flux distribution on Solar Tower receivers by interpolation of few discrete representations. *Sol. Energy* 160, 43–55.
- Schöttl, P., Bern, G., van Rooyen, D., Heimsath, A., Fluri, T., Nitz, P., 2017. Solar tower cavity receiver aperture optimization based on transient optical and thermo-hydraulic modeling. In: SOLARPACES 2016: International Conference on Concentrating Solar Power and Chemical Energy Systems. AIP Conference Proceedings.
- Schöttl, P., Ordóñez Moreno, K., van Rooyen, D., Bern, G., Nitz, P., 2016. Novel sky discretization method for optical annual assessment of solar tower plants. *Sol. Energy* 138, 36–46.
- Siebers, D.L., Kraabel, J.S., 1984. Estimating Convective Energy Losses From Solar Central Receivers. Tech. Rep. SAND-84-8717, Sandia National Laboratories.
- Smith, D.C., 1992. Design and optimization of tube-type receiver panels for molten salt application. *Sol. Eng.* 2, 1029–1036.
- Teichel, S.H., Feierabend, L., Klein, S.A., Reindl, D.T., 2012. An alternative method for calculation of semi-gray radiation heat transfer in solar central cavity receivers. *Sol. Energy* 86 (6), 1899–1909.
- Theano Development Team, 2016. Theano: A Python framework for fast computation of mathematical expressions. arXiv e-prints abs/1605.02688.
- Tilley, D., Kelly, B., Burkholder, F., 2014. Baseload nitrate salt central receiver power plant design.
- VDI-GVC, 2010. VDI Heat Atlas: Verein Deutscher Ingenieure, VDI-Gesellschaft Verfahrenstechnik und Chemieingenieurwesen (CVG), 2nd Edition. Springer Verlag, Berlin and Heidelberg.
- Wang, K., He, Y.-L., Li, P., Li, M.-J., Tao, W.-Q., 2017. Multi-objective optimization of the solar absorptivity distribution inside a cavity solar receiver for solar power towers. *Sol. Energy* 158, 247–258.
- Wittwer, C., 1999. ColSim - Simulation von Regelungssystemen in aktiven solarthermischen Anlagen. Ph.D. thesis. Universität Karlsruhe, Fakultät für Architektur.
- Yang, X., Yang, X., Ding, J., Shao, Y., Fan, H., 2012. Numerical simulation study on the heat transfer characteristics of the tube receiver of the solar thermal power tower. *Appl. Energy* 90 (1), 142–147.
- Zou, C., Zhang, Y., Falcoz, Q., Neveu, P., Zhang, C., Shu, W., Huang, S., 2017. Design and optimization of a high-temperature cavity receiver for a solar energy cascade utilization system. *Renew. Energy* 103, 478–489.